

Design of Efficient Artificial Enzymes Using Crystallographically Enhanced Conformational Sampling

Rojo V. Rakotoharisoa, Behnoush Seifnoferest, Niayesh Zarifi, Jack D.M. Miller, Joshua M. Rodriguez, Michael C. Thompson,* and Roberto A. Chica*



Cite This: *J. Am. Chem. Soc.* 2024, 146, 10001–10013



Read Online

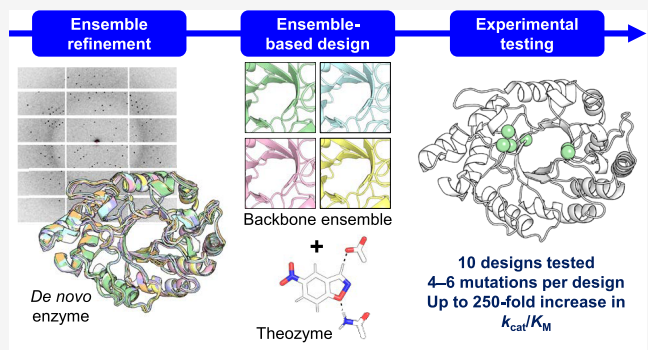
ACCESS |

Metrics & More

Article Recommendations

Supporting Information

ABSTRACT: The ability to create efficient artificial enzymes for any chemical reaction is of great interest. Here, we describe a computational design method for increasing the catalytic efficiency of de novo enzymes by several orders of magnitude without relying on directed evolution and high-throughput screening. Using structural ensembles generated from dynamics-based refinement against X-ray diffraction data collected from crystals of Kemp eliminases HG3 (k_{cat}/K_M 125 M⁻¹ s⁻¹) and KE70 (k_{cat}/K_M 57 M⁻¹ s⁻¹), we design from each enzyme ≤ 10 sequences predicted to catalyze this reaction more efficiently. The most active designs display k_{cat}/K_M values improved by 100–250-fold, comparable to mutants obtained after screening thousands of variants in multiple rounds of directed evolution. Crystal structures show excellent agreement with computational models, with catalytic contacts present as designed and transition-state root-mean-square deviations of ≤ 0.65 Å. Our work shows how ensemble-based design can generate efficient artificial enzymes by exploiting the true conformational ensemble to design improved active sites.



INTRODUCTION

The ability to create efficient artificial enzymes for any desired chemical reaction is of great interest as it would open the door to a broad range of applications in industry and medicine. Algorithms for de novo enzyme design^{1,2} can be used to create artificial enzymes for reactions for which no naturally occurring enzyme is known. While this computational design process has been used to produce de novo enzymes for various model organic transformations,^{3–7} downstream directed evolution has been necessary to convert these enzyme prototypes into catalysts as efficient as their natural counterparts.^{8–13} However, directed evolution is time-consuming and impractical for many enzymatic reactions of interest, for which high-throughput screening assays are unavailable. Therefore, a computational design procedure to enhance the catalytic efficiency of de novo enzymes would be beneficial as it could bypass directed evolution and accelerate the creation of efficient artificial enzymes.

Structural analyses of high-activity variants evolved from de novo enzymes revealed several mechanisms by which catalytic functions can be augmented. These mechanisms include optimization of hydrogen-bond geometries between catalytic residues and the transition state (TS),⁸ enhancement of active-site complementarity to the TS,^{8,9,14} improvement of active-site preorganization,¹⁴ and enrichment of catalytically competent substates in the conformational ensemble.^{15–17} These

structural effects are challenging to design using current enzyme design protocols^{3,7,9} because they are not sufficiently precise⁸ and do not consider the dynamic nature of enzyme structures.¹⁵ Recently, new methodologies have been developed that take advantage of the spatiotemporal averaging inherent to X-ray crystallography—crystallographic data represent billions of crystallized molecules that are all sampling different conformations during data collection—to model the conformational ensembles of proteins with high fidelity.^{18,19} New design strategies that could exploit this experimental information should facilitate the design of efficient artificial enzymes by enabling the accurate modeling of catalytically productive conformational substates.

Here, we report a computational procedure for enhancing the catalytic efficiency of de novo enzymes that exploits crystallographically derived ensemble models for increased accuracy. Starting from the noncryogenic crystal structure of de novo Kemp eliminase HG3,^{7,14} we generate a structural ensemble fitted to the diffraction data^{18,20} and use it to design

Received: January 15, 2024

Revised: March 12, 2024

Accepted: March 13, 2024

Published: March 27, 2024



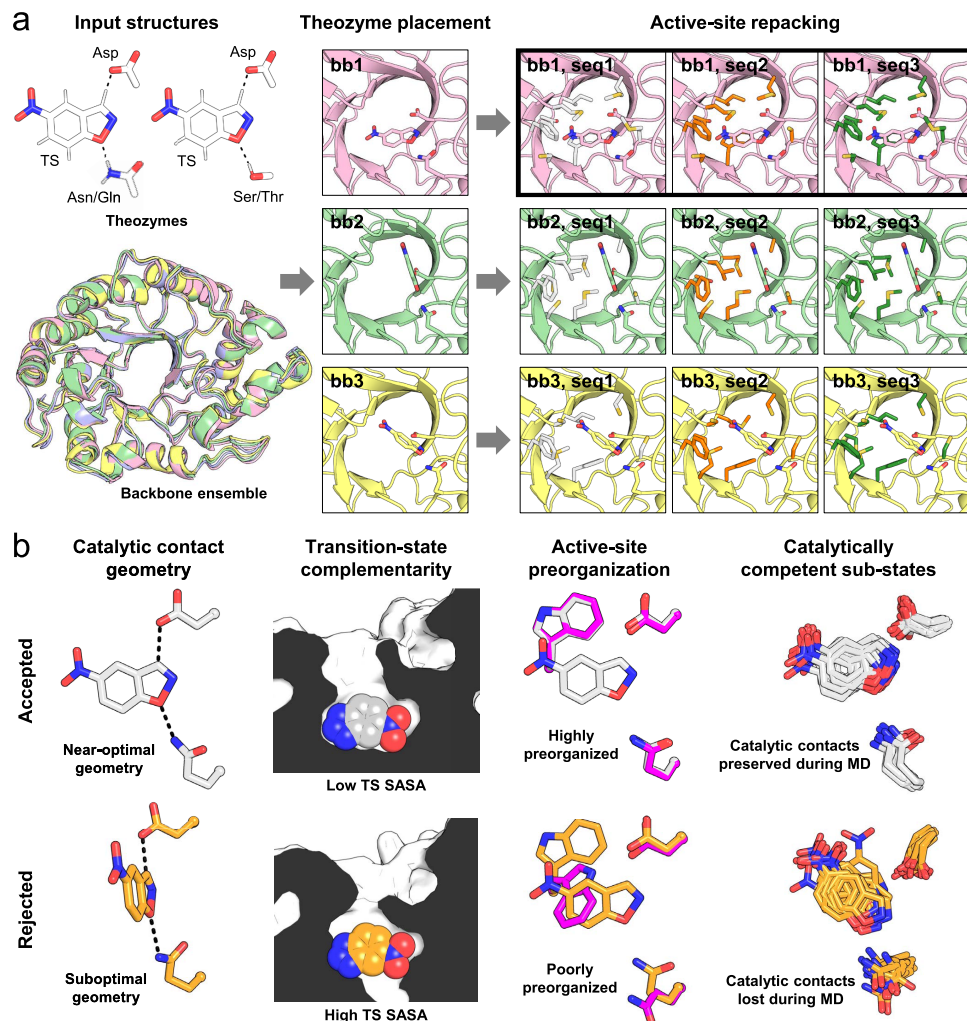


Figure 1. Ensemble-based computational enzyme design. (a) This procedure requires as inputs one or more theozymes, which are combinations of catalytic groups arranged in a unique geometry to stabilize a TS, and a backbone ensemble that approximates the intrinsic flexibility of the target protein fold. The algorithm proceeds in two stages: placement of each theozyme onto every member of the backbone ensemble (bb1–3), followed by repacking of active-site residues to identify sequences (seq1–3) that can further stabilize the TS. During repacking, both the identity and conformation of designed active-site residues are allowed to vary, and the TS is rotated and translated to reduce steric clashes with repacked side chains. In this toy example, only the theozyme containing a Gln hydrogen-bond donor is shown for the sake of clarity. After active-site repacking, designs from single theozyme/template combinations are selected based on energy (bold outline) and filtered using structural criteria. (b) Filtering of designs is performed to reproduce structural features that have previously been associated with efficient catalysis in other Kemp eliminases. Accepted designs are those that have (1) near-ideal contact geometries between the TS and catalytic side chains (dashed lines), (2) active sites with high structural complementarity to the TS, as calculated by low TS solvent-accessible surface area (SASA), (3) highly preorganized active sites with most designed residues predicted to adopt the same rotameric configuration in the presence (white/orange) and absence (magenta) of TS, and (4) enriched catalytically competent substates, which are snapshots that preserve catalytic contacts over the course of short molecular dynamics (MD) simulations.

mutant sequences predicted to efficiently catalyze the Kemp elimination. We filter these sequences using a variety of structural criteria aiming to reproduce molecular mechanisms known to augment enzyme catalysis and experimentally characterize 10 sequences. The most active design displays a catalytic efficiency improved by approximately 250-fold, a result comparable to those obtained by seven rounds of directed evolution and screening of >7000 variants.⁸ We solve crystal structures of several high-activity variants that show excellent agreement with the computational models and confirm that catalytic efficiency is enhanced via the intended molecular mechanisms. We also apply our approach to another *de novo* Kemp eliminase, KE70,³ which yields comparable results. Our work shows how ensemble-based design can

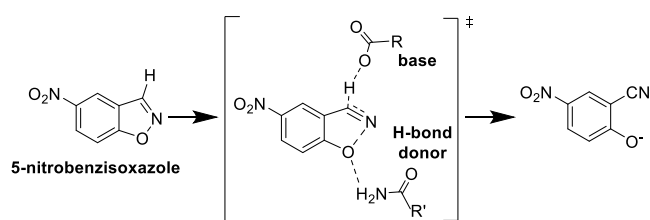
generate efficient artificial enzymes by exploiting information derived from X-ray crystallography to identify productive substates for efficient catalysis.

RESULTS

Ensemble-Based Enzyme Design. To create efficient *de novo* enzymes without relying on iterative rounds of mutagenesis and high-throughput screening, we implemented an ensemble-based computational enzyme design pipeline that uses protein backbones generated by ensemble refinement of diffraction data¹⁸ as templates for design (Figure 1). Because the diffraction data and calculated electron density maps are derived from crystals that contain billions of molecules, which are all sampling different conformational states throughout

data collection, the resulting ensemble models represent a distribution of conformations that are well populated in the ensemble at equilibrium.²¹ Thus, we postulated that performing crystallographic ensemble refinement on a low activity de novo enzyme would allow sampling of conformational substates that can more accurately accommodate the TS and its interactions with catalytic residues than the single conformation modeled using traditional refinement methods, thereby facilitating the design of improved active sites. To test our hypothesis, we applied an ensemble-based design to increase catalytic efficiency of the de novo enzyme HG3⁷ that catalyzes the Kemp elimination (Scheme 1), a well-established

Scheme 1. Reaction Catalyzed by HG-Series Kemp Eliminases



model organic transformation for benchmarking computational enzyme design methods. We selected HG3 as the case study for three reasons. First, X-ray diffraction data collected at noncryogenic temperatures (277 K) were available,¹⁴ which is ideal for ensemble refinement because cryocooling is known to narrow the conformational ensemble of crystallized proteins,²² reducing the number of conformations that are represented in the ensemble-averaged data. Second, these data were collected from crystals with a bound TS analogue that is resolved in the electron density,¹⁴ allowing inclusion of the TS in the ensemble models. Finally, HG3 was subjected to an extensive directed evolution campaign that increased catalytic efficiency by almost 3 orders of magnitude,⁸ allowing us to compare results with those from purely experimental approaches.

We generated an ensemble of 84 backbone templates (Supplementary Table 1) from the crystal structure of HG3 bound with the 6-nitrobenzotriazole (6NT, Supplementary Figure 1) TS analogue (PDB ID: 5RGA¹⁴) and used these structures for placement of four theozymes containing an Asp residue as catalytic base, and either Gln, Asn, Ser, or Thr (Figure 1a) to stabilize the binding of the substrate and properly orient it for reaction with the base. We kept the base position fixed to that of HG3 (D127) but allowed the algorithm to place the hydrogen-bond donor at multiple positions in the active site given that no amino acid residue in HG3 forms this catalytic contact with 6NT.¹⁴ We then repacked the active site around the most stable theozyme placed on each backbone template by optimizing the identity and side-chain conformation of residues within 4 Å of the TS and catalytic residues (Supplementary Table 2) to maximize beneficial nonbonding interactions with the theozyme, which has been shown to contribute to increased catalytic activity.⁸

After repacking, we filtered designs using a series of structural metrics aiming to reproduce mechanisms known to augment enzyme catalysis (Figure 1b, Supplementary Table 3). First, we measured angles defining the hydrogen bond between D127 and the TS for the top-scoring design obtained on each backbone template, and selected sequences from the single backbone template that gave the most stable design with angles

that were closest to the optimal geometries calculated for acetamide dimers²³ (Supplementary Figure 2, Supplementary Table 4), which mimic the geometry needed for efficient proton transfer. The selected backbone, which we name bb05, yielded sequences that contain the Q50 hydrogen-bond donor that emerged during evolution of HG3 and that is present in the highest activity variants of this enzyme family.⁸ Second, we evaluated active-site complementarity to the TS by calculating the solvent-accessible surface area of this ligand in the computational models generated for 1000 sequences designed on backbone bb05. Only designs where ≥95% of the TS surface is buried were kept. Third, we evaluated active-site preorganization by calculating the percentage of designed active-site residues that were predicted to adopt similar rotamers in the absence and presence of the TS. Sequences whose active sites were predicted to be >70% preorganized were kept. We also eliminated sequences with calculated energies over 10 kcal mol⁻¹ higher than that of an HG3 single point mutant containing the D127/Q50 catalytic dyad as well as those that contained more than four methionines or more than one cysteine in the active site to avoid excessive conformational heterogeneity and prevent formation of disulfide bonds, respectively. Importantly, we did not eliminate entirely these amino acids from our designed active sites nor explicitly specify which positions should contain the methionines or cysteine that were preserved. This filtering process narrowed the original list of 1000 designs obtained from backbone bb05 down to 55 designs. A final filtering step consisting of a 20 ns MD simulation was used to identify designs that were enriched in catalytically competent conformational substates, which we define as snapshots that make the designed catalytic contacts (Supplementary Figure 3). This final filtering resulted in nine sequences containing four or five mutations (Table 1), which we experimentally characterized.

Kinetic Characterization of Designs. All nine designs catalyzed the Kemp elimination (Supplementary Figure 4), with all but two having catalytic efficiencies greater than that of HG3 (Table 1). The most active of these variants, HG630, had a catalytic efficiency of $15,000 \pm 500 \text{ M}^{-1} \text{ s}^{-1}$, a value that is 120-fold higher than that of the starting template HG3. Furthermore, the three most active designs (HG198, HG259, and HG630) were more catalytically efficient than the HG3.3b variant obtained after three rounds of directed evolution and screening of >3000 mutants.⁸ These designs all contain the M84C mutation that was previously shown to increase catalytic efficiency by 1 order of magnitude when combined with K50Q to yield the HG3-KS0Q/M84C double mutant¹⁵ (Table 1). Comparison of the sequences of HG44 and HG57, which differ by a single point mutation at position 90, suggested that the introduction of the Q90F mutation into HG630 would further enhance its catalytic efficiency as it doubles k_{cat}/K_M when introduced into HG57 to yield HG44. Introduction of this mutation into HG630 doubled its catalytic efficiency and resulted in a hexamutant (HG649) that is 256-fold more catalytically efficient than HG3 ($k_{\text{cat}}/K_M = 32,000 \pm 3000 \text{ M}^{-1} \text{ s}^{-1}$) and more active than HG3.7, a variant found after seven rounds of directed evolution involving the screening of >7000 mutants⁸ (Table 1, Figure 2a). HG649 shares a majority of its mutation sites with HG3.7, but the combination of specific amino acid substitutions is distinct with only two mutations in common (Figure 2b). These results demonstrate how ensemble-based enzyme design produces similar activity

Table 1. Kinetic Parameters of Kemp Eliminases

enzyme	mutations ^a	#mutations ^a	k_{cat} (s^{-1}) ^b	K_M (mM) ^b	k_{cat}/K_M ($\text{M}^{-1} \text{s}^{-1}$) ^b	relative k_{cat}/K_M
HG series – controls						
HG3			N.D.	N.D.	125 ± 8 (146 ± 6) ^c	1
HG3.3b	V6I K50H M84C S89R Q90D A125N	6	N.D.	N.D.	3400 ± 700 (2200 ± 100) ^c	27
HG3-K50Q/M84C	K50Q M84C	2	N.D.	N.D.	4300 ± 300	34
HG3.7	V6I Q37K K50Q M84C S89R Q90H A125N	7	N.D.	N.D.	$24,000 \pm 3000$ ($27,000 \pm 2000$) ^c	192
HG series – designs						
HG378	A21C K50Q Q90L A125V W275V	5	N.D.	N.D.	70 ± 5	0.6
HG57	A21C K50Q Q90L A125V	4	N.D.	N.D.	120 ± 8	1
HG44	A21C K50Q Q90F A125V	4	N.D.	N.D.	250 ± 10	2
HG603	K50Q Q90F A125V W275V	4	N.D.	N.D.	800 ± 10	6.4
HG493	K50Q Q90F A125T W275T	4	N.D.	N.D.	2100 ± 100	17
HG185	A21C K50Q Q90F A125T W275V	5	N.D.	N.D.	2300 ± 100	18
HG198	K50Q M84C A125T F267M	4	N.D.	N.D.	8000 ± 300	64
HG259	K50Q M84C Q90L A125T F267M	5	N.D.	N.D.	$13,000 \pm 400$	104
HG630	K50Q M84C A125T F267M W275V	5	N.D.	N.D.	$15,000 \pm 500$	120
without MD filtering ^d						
HG649	K50Q M84C Q90F A125T F267M W275V	6	N.D.	N.D.	$32,000 \pm 3000$	256
KE70 series – controls						
KE70			N.D.	N.D.	57 ± 3 (78 ± 14) ^c	1
KE70-S20a/A240a ^e	S20a A240a	2	N.D.	N.D.	150 ± 7	2.6
R2 7/12F	D23G, Y48F, D212E, H251Y	4	0.50 ± 0.01	1.00 ± 0.06	500 ± 30 (1330 ± 13) ^c	9
R4 8/5A ^e	S20a, K29N, Y48F, W72C, H166Y, K197N, A204V, G240a	8	3.0 ± 0.1	1.0 ± 0.1	3000 ± 300 (4380 ± 350) ^c	53
KE70 series – designs ^f						
KE701 ^e	H16D S20a D45Q Y48F W72C G101S S138Q H166N V168A A204V A240a	11	0.040 ± 0.001	0.10 ± 0.02	400 ± 80	7
KE703 ^e	H16D S20a D45N Y48F W72V G101M S138Q H166N V168A A204V A240a	11	0.50 ± 0.01	0.20 ± 0.02	2500 ± 300	44
KE703b ^e	S20a Y48F W72V G101M S138Q H166N V168A A204V A240a	9	N.D.	N.D.	5500 ± 100	96

^aMutations are relative to the starting template (HG3 or KE70). ^bData represent the average of six to 12 individual replicate measurements from two to four independent protein batches. N.D. indicates that individual parameters K_M and k_{cat} could not be determined accurately because saturation was not possible at the maximum substrate concentration tested (2 mM, *Supplementary Figures 4 and 5*), which is the substrate's solubility limit. In these cases, catalytic efficiencies (k_{cat}/K_M) were calculated from the slope of the linear portion ($[S] \ll K_M$) of the Michaelis–Menten model ($v_0 = (k_{\text{cat}}/K_M)[E_0][S]$). Errors of regression fitting, which represent the absolute measure of the typical distance that each data point falls from the regression line, are provided. ^cValues in parentheses are from Broom et al.¹⁴ (HG series), or Röthlisberger et al.³ and Khersonsky et al.¹⁰ (KE70 series). ^dHG649 is one of the 55 designs that passed all filtering criteria prior to the final MD step. ^eThese enzymes contain two insertions, S20a and A240a/G240a. ^fThe KE702 design was inactive.

increases as directed evolution but without extensive experimental screening. Interestingly, HG649 was one of the 55 designs that passed all filtering criteria except for the final MD analysis, which led to its elimination due to its low predicted catalytic competency (*Supplementary Figure 3*). This false negative, along with the two false positives (*Table 1*, HG378 and HG57), indicates that improvements are required to make the MD filtering more robust, for example, by running multiple replicas and/or longer simulations, and suggests that other eliminated sequences may also display high catalytic efficiency.

Crystal Structures. To evaluate whether the catalytic efficiency of our designs was increased via the predicted molecular mechanisms (*Figure 1b*), we solved room-temperature (280 K) X-ray crystal structures of four of the most active designs (HG185, HG198, HG630, and HG649) in the

presence and absence of the 6NT TS analogue. We determined structures at room temperature for direct comparison with the HG3 noncryogenic structure used to generate the ensemble and because this method can reveal conformational heterogeneity in protein structures that would not be visible at cryogenic temperatures, providing insights into the conformational ensemble that is sampled by a protein.^{21,24} Crystals of HG185, HG630, and HG649 were obtained in the absence of 6NT and soaked into solutions containing this molecule prior to X-ray data collection to obtain the bound structures (*Supplementary Table 5*). These three enzyme variants all crystallize in space group $P2_1$ with two molecules in the asymmetric unit, roughly matching the crystal form reported for HG3.¹⁴ On the other hand, HG198 could only be crystallized in the presence of 6NT, and its unbound structure was derived from serially soaking these crystals in solutions

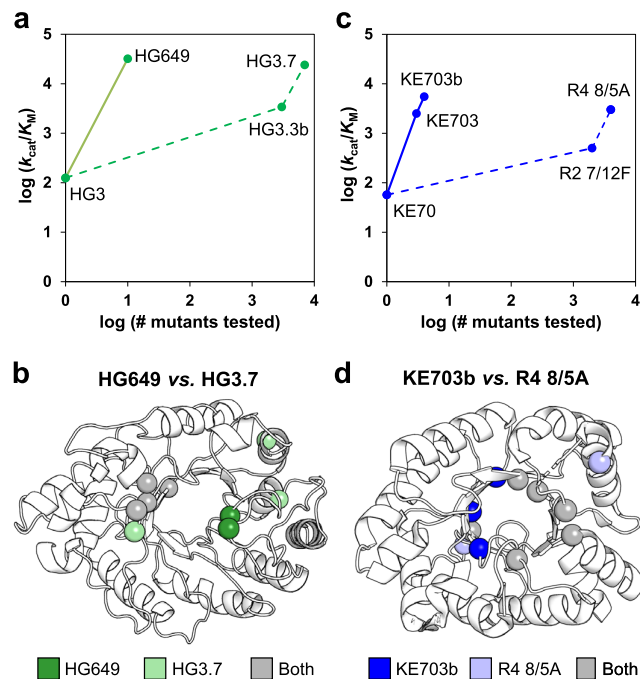


Figure 2. Ensemble-based design vs directed evolution. (a) Ensemble-based design yields catalytic efficiency improvements comparable to those achieved by directed evolution with a fraction of the experimental screening effort. Full and dashed lines show ensemble-based design and directed evolution trajectories, respectively. (b) Ensemble-based design identifies a majority of the mutation sites (spheres) found by directed evolution (4/6) but mutation combinations of designed (HG649) and evolved (HG3.7) enzymes are distinct as these share only two mutations (K50Q and M84C). (c) Full and dashed lines show ensemble-based design and directed evolution trajectories, respectively. KE703b differs from KE703 by reversion of its D16/N45 residues to the H16/D45 catalytic dyad found in KE70 and its evolved variants. (d) Designed variant KE703b shares 6 of the 9 mutation sites (spheres) found by directed evolution but has only three mutations in common with evolved variant R4 8/5A (S20a, Y48F, A204V).

lacking the TS analogue prior to data collection. In the presence of 6NT, HG198 crystallizes in low symmetry space group $P1$ with three molecules in the asymmetric unit, but removing the TS analogue via serial soaking transforms the crystals to space group $P2_1$ with a single molecule in the asymmetric unit. This unusual transformation of the crystal system was consistent over multiple crystal specimens. All crystals diffracted at resolutions of 1.32–1.90 Å, which enabled us to create high-quality structural models (Supplementary Table 6).

All designs bound 6NT in the same catalytically productive pose (Figure 3a) as that observed in HG3, in excellent agreement with the computational models generated by ensemble-based design but in stark contrast with those generated using the average crystal structure (Figure 4), highlighting the increased accuracy afforded by the use of a crystallographically derived ensemble.¹⁴ In this pose, the acidic N–H bond of 6NT that mimics the cleavable C–H bond of the substrate is located within hydrogen-bonding distance to the carboxylate oxygen of D127, while the basic nitrogen atom corresponding to the phenolic oxygen of the TS forms a hydrogen bond with the N_e atom of Q50, similar to what was observed for evolved variant HG3.7.¹⁴ By contrast, HG3 does

not form this second hydrogen bond because its K50 residue does not adopt a suitable side-chain conformation, and instead, it is a water molecule that hydrogen bonds to the basic nitrogen atom of 6NT. In all cases, angles defining the hydrogen bond between D127 and the TS analogue were improved or within error compared to HG3 (Supplementary Table 4). In contrast to all other enzymes, the 6NT TS analogue of HG185 was refined to an occupancy of approximately 60%, indicating that its crystal comprises a mixture of enzyme molecules in their bound and unbound forms. Given that the soaking procedure we used to generate crystals of HG185 bound to 6NT was identical to the one used to soak isomorphous crystals of HG630 and HG649 (Supplementary Table 5), which yielded 6NT bound at 100% occupancy, it is likely that the lower occupancy of this ligand in HG185 reflects its weaker binding in the active site, in agreement with the enzyme's 6.5–14-fold lower catalytic efficiency compared to HG630 and HG649 (Table 1). The lower occupancy of 6NT in the HG185 structure is reflected by the weaker electron density in the active site and the presence of an alternate D127 rotamer that does not hydrogen bond with the TS analogue (Figure 3a). Regardless, the active site of all designed variants is more complementary to the TS than that of HG3, as indicated by the lower solvent-accessible surface area for 6NT when bound in the active site of these variants (Figure 3b).

Next, we evaluated active-site preorganization, which is an important contributor to enzyme catalysis,²⁵ by comparing structures in the presence and absence of bound 6NT. In HG3, the unbound form is not preorganized for catalysis as both W44 and M237 adopt conformations that would prevent productive binding of 6NT in the major or minor conformations, respectively (Figure 3c). This is also the case for evolved variant HG3.7.¹⁴ HG185 is also poorly preorganized in the unbound form because C21 exclusively adopts a rotamer that would clash with 6NT. Furthermore, the D127 catalytic residue of HG185 adopts a low occupancy (7 and 14% for chains A and B, respectively), catalytically nonproductive conformation in the unbound form that cannot interact favorably with 6NT, likely contributing to its inferior activity compared with the other variants. By contrast, active sites of higher activity variants HG198, HG630, and HG649 are correctly preorganized for catalysis in a substantial portion of the molecules in the crystal, with only M237 adopting a nonproductive conformation at 47–64% occupancy (Figure 3c). Overall, crystal structures confirmed that the activity of designed HG variants was increased by several of the mechanisms known to enhance enzyme catalysis and that we aimed to reproduce using our filtering criteria.

Enrichment of Catalytically Competent Substates.

The ability of an enzyme to frequently sample productive substates in its conformational ensemble is another important feature of efficient catalysis.^{15,17,26,27} To evaluate this property for our designs, we performed ensemble refinement of their 6NT-bound structures and evaluated the proportion of ensemble members that make the designed catalytic contacts with the TS analogue. We observed that in HG3, the hydrogen bond between the catalytic base and 6NT is formed in 82% of ensemble members and no interaction is observed between the ligand and K50 (Figure 3d). In HG185, interactions between 6NT and catalytic residues D127 and Q50 are present in 45 and 65% of ensemble members, respectively, likely due to the lower occupancy of 6NT. In the case of the most active

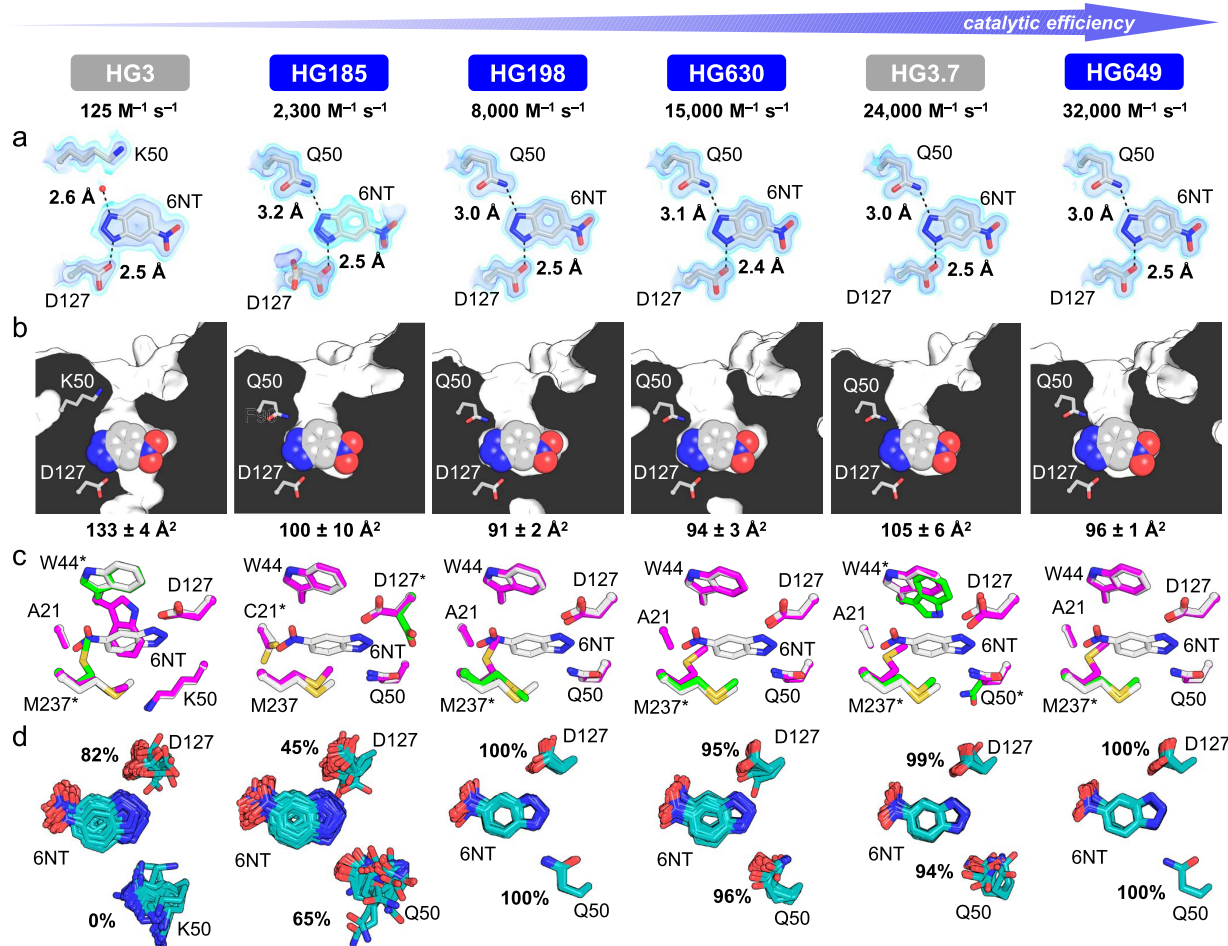


Figure 3. Crystal structures of HG series Kemp eliminases. In all cases, only atoms from chain A are shown. Structures of HG3 (PDB ID: 5RG4 and 5RGA) and its evolved variant HG3.7 (PDB ID: 5RG6 and 5RGC) were previously published.¹⁴ (a) Hydrogen bonds to the 6-benzotriazole (6NT) TS analogue are shown as dashed lines, and distances are indicated. Hydrogen bond angles are listed in *Supplementary Table 14*. The red sphere represents a water molecule. The 2Fo-Fc map is shown in volume representation at two contour levels: 0.5 and 1.5 e Å⁻³ in light and dark blue, respectively. In the case of HG185, occupancy of 6NT in the crystal is approximately 60%, which is reflected by its lower electron density. (b) Cutaway view showing that active sites of designs are more complementary to the TS analogue than that of the HG3 template, as indicated by lower solvent-accessible surface areas for 6NT (mean ± s.d. across all chains). 6NT is shown as spheres. (c) Superposition of the 6NT-bound structure (white) with the highest (magenta) and lowest (green) occupancy conformers of the unbound structure for each Kemp eliminase. Active-site residues that are not preorganized are indicated by an asterisk. In the starting template HG3 and evolved variant HG3.7, the unbound state is not preorganized for catalysis as both W44 and M237 in the major and minor conformers, respectively, adopt side-chain rotamers that would prevent productive binding of the TS. In the HG185 design, the electron density for C21 in the unbound state reveals a single side-chain conformation that overlaps with the space occupied by the TS analogue in the bound state, demonstrating that it is not preorganized for catalysis. In the HG198, HG630, and HG649 designs, only M237 adopts a nonproductive conformation in the unbound state, with an occupancy ranging from 47 to 64%. (d) Ensemble refinement of 6NT-bound structures shows that designed variants HG198, HG630, and HG649, as well as evolved variant HG3.7, display lower structural heterogeneity than HG3 and a higher percentage of ensemble members whose catalytic side chains (D127 and Q50) make hydrogen bonds with 6NT. In the case of HG185, the lower occupancy of 6NT in the crystal (approximately 60%) likely contributes to its comparable heterogeneity to HG3 and lower percentage of ensemble members making catalytic contacts with 6NT.

variants HG198, HG630, and HG649, catalytic contacts to both D127 and Q50 are presented in ≥95% of ensemble members, and their ensembles are less structurally diverse than those of HG3 or HG185 (*Figures 3d* and *5a*, *Supplementary Table 7*). The higher percentage of hydrogen bonds between 6NT and catalytic residues, and narrower conformational ensembles of high-activity HG variants whose structures contain TS analogues at 100% occupancy, confirm a population of catalytically competent substates higher than in the ensemble of HG3.

Next, we quantified the extent to which ensemble-based design was able to shift the conformational ensemble observed for HG3 by analyzing the crystallographic ensemble models of

the 6NT-bound forms of HG3 and the efficient HG variants that bound this TS analogue with 100% occupancy (HG198, HG630, and HG649). First, we calculated the pairwise backbone root-mean-square deviations (RMSDs) for all pairs of structures within a single ensemble model and plotted their distributions (*Figure 5a*). Comparing the more active variants to HG3 demonstrated that all of these improved enzymes have a narrower (more self-consistent) ensemble, whose members have a lower median pairwise RMSD (*Supplementary Table 7*), which decreases as catalytic efficiency increases (e.g., 0.22, 0.17, 0.12, and 0.09 Å for HG3, HG198, HG630, and HG649, respectively). Next, we wanted to ask whether the ensembles of the more active variants are converging on the most highly

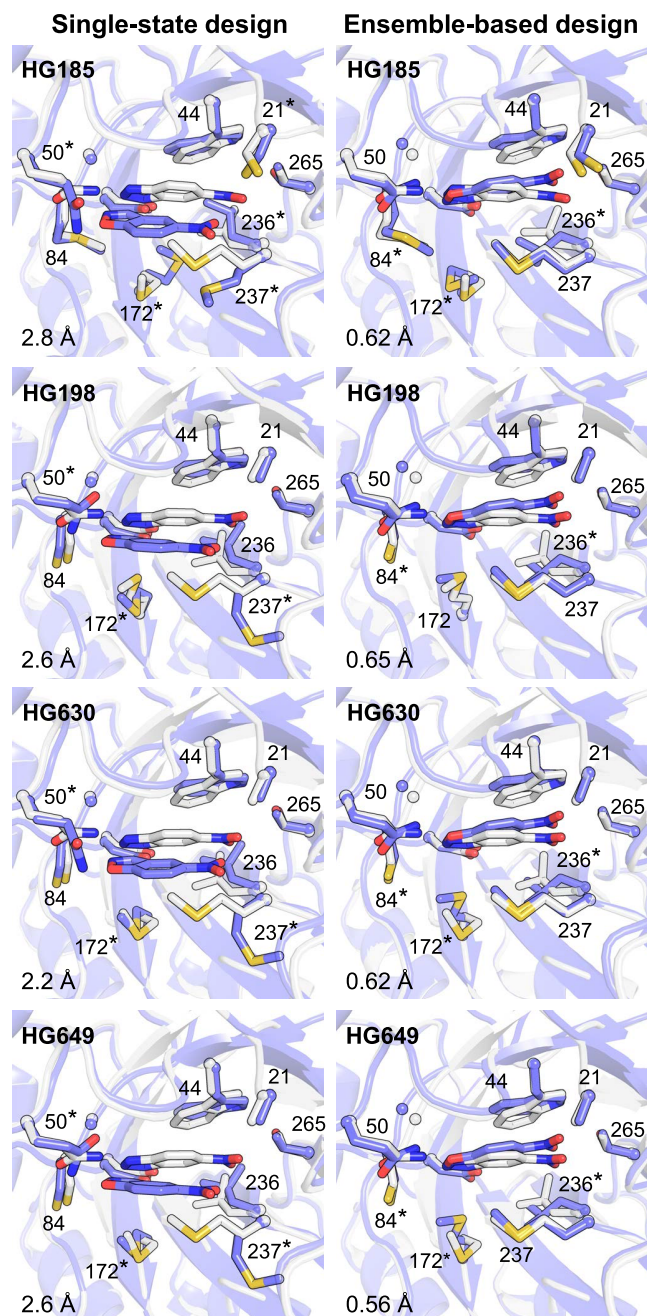


Figure 4. Computational models vs crystal structures. Crystal structures of HG-series Kemp eliminases with bound 6NT (white) are overlaid on the corresponding design models obtained by single-state design with the average crystal structure or ensemble-based design (blue). For clarity, only the major conformer of Chain A is shown. Root-mean-square deviations between the TS in the design models and the TS analogue in corresponding crystal structures are indicated at the bottom left. The TS and TS analogue are shown at the center of each image. Side chains of all residues forming the binding pocket are shown with the exception of P45, which was omitted for clarity. The sphere shows the α carbon of G83. Asterisks indicate residues that adopt side-chain rotamers varying by $>20^\circ$ around one or more side-chain dihedrals between the design model and crystal structure.

populated conformations in the HG3 ensemble or around a different subset of conformations that might provide a better active-site structure. To assess this, we calculated the pairwise RMSD between the single conformer structure of HG3 bound

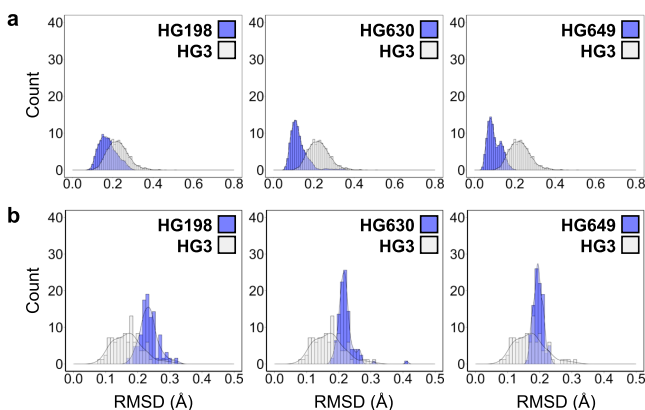


Figure 5. Ensemble-based design leads to a shift in the conformational ensemble. (a) Distributions of pairwise backbone RMSDs are calculated for all pairs of structures within a single ensemble model. Comparing the distributions derived from efficient HG variants (HG198, HG630, and HG649) bound to 6NT (blue) with those derived from the HG3 ensemble model, also with bound 6NT (white), reveals that the design process leads to a narrower (more self-consistent) distribution of conformations with a lower median pairwise RMSD. This effect is most pronounced for the most active variants (HG630 and HG649). (b) Distributions of pairwise RMSD between the single conformer structure of HG3 (PDB ID: SRGA¹⁴) and the individual members of various ensemble models demonstrate that the ensembles of the improved variants have evolved to include conformations that are significantly different from HG3. RMSD values are calculated over active-site residues listed in *Supplementary Table 2*. Median RMSD values and Z-scores for comparison of distributions are reported in *Supplementary Table 7*.

to 6NT (PDB ID: SRGA¹⁴) and the individual members of various ensemble models (HG198, HG630, HG649, and HG3). We observed that the single conformer structure of HG3 has a lower median RMSD relative to members of the HG3 ensemble model (0.17 \AA) than it does relative to structures present in the ensemble models corresponding to higher activity variants ($0.19\text{--}0.23\text{ \AA}$, *Figure 5b*, *Supplementary Table 7*). Taken together, these RMSD calculations suggest that our design procedure narrows the ensembles of the more active variants around conformations that are substantially different from those that are most frequently populated by HG3.

KE70 Designs. To further test our ensemble-based enzyme design method, we applied it to another Kemp eliminase that was designed on a different protein scaffold. This enzyme, KE70, contains a His/Asp dyad that acts as catalytic base and a Ser hydrogen-bond donor to stabilize productive substrate binding.³ To allow direct comparison to our HG enzymes, we designed variants using a theozyme comprising an Asp residue as a catalytic base and a Gln as a hydrogen-bond donor. Starting from the available unbound cryogenic crystal structure of KE70 (PDB ID: 3NPV¹⁰), we generated an 84-member ensemble (*Supplementary Table 1*) and used it to design variants predicted to efficiently catalyze the Kemp elimination using a similar protocol as that used for HG enzymes but without the final filtering step involving MD (Methods section). Three variants were selected for kinetic analysis, and these contain between 11 and 13 mutations (*Supplementary Table 8*), including the D16 and Q138 catalytic motif as well as two insertions in active-site loops (S20a and A240a) that we added after design. These loop insertions were manually introduced into KE70 during its directed evolution,¹⁰

and we added them to allow for direct comparison with evolved KE70 variants that contain these insertions, which increase the catalytic efficiency by 2.6-fold when introduced on their own into KE70 (Table 1). Two of the three tested designs were active (Supplementary Figure 5). The most active variant, KE703, displays a k_{cat}/K_M value of $2500 \pm 300 \text{ M}^{-1} \text{ s}^{-1}$, which is 44-fold higher than KE70 and approximately 17-fold higher than that of a KE70 variant containing the two loop insertions (Table 1). To compare with evolved KE70 variants that contain the His/Asp dyad as a catalytic base, we introduced the D16H and N45D mutations into KE703, generating the KE703b variant. This variant has a k_{cat}/K_M value of $5500 \pm 100 \text{ M}^{-1} \text{ s}^{-1}$, which is approximately 100-fold higher than KE70 and 2-fold higher than that of the evolved variant R4 8/5A that was isolated after 4 rounds of directed evolution and screening of approximately 4000 clones¹⁰ (Figure 2c). KE703b shares a majority of its mutation sites with R4 8/5A, but its specific amino-acid substitutions are distinct, with only three mutations in common (Figure 2d). These results confirm the ability of ensemble-based design to generate artificial enzymes that are orders of magnitude more active than the original de novo enzymes at a fraction of the experimental effort required by directed evolution. Furthermore, our results show that ensemble-based design does not require an ensemble generated from a room-temperature crystal structure with a bound TS analogue to be successful, which is advantageous given that such structures are less common than unbound ones solved at a cryogenic temperature.

DISCUSSION

In this work, we used ensemble-based computational design to increase the catalytic efficiency of the HG3 and KE70 de novo Kemp eliminases by 2 orders of magnitude, yielding artificial enzymes with k_{cat}/K_M values that are only 4- or 10-fold lower than those of the most active variants evolved from these enzyme prototypes (e.g., k_{cat}/K_M of 126,000 and 53,100 $\text{M}^{-1} \text{ s}^{-1}$ for HG3.17¹⁴ and KE70 R8 12/12B¹⁰, respectively). To achieve these results, we tested a number of variants that are several orders of magnitude lower than those previously used to achieve comparable improvements by directed evolution.^{8,10} The success of our ensemble-based design relied on exploiting the spatiotemporally averaged information contained in X-ray crystallographic data to overcome the backbone sampling challenge that is responsible for much inaccuracy in enzyme design.⁸ While others have previously attempted to address the backbone sampling issue by using ensembles generated via Monte Carlo-based backrub sampling and incorporating loop remodeling during the enzyme design process, activity improvements were modest (<5-fold).¹⁰ These results, in combination with our previous observation that use of an ensemble generated by unconstrained MD does not allow accurate recapitulation of catalytic contact and active-site configurations for an efficient artificial enzyme,¹⁴ suggest that to obtain large activity increases, it is not sufficient to introduce backbone flexibility in the design process. Instead, the correct backbone conformation must be sampled. Crystallographic ensemble refinement of the initial de novo enzyme satisfies this stringent requirement in that the resulting model represents the true conformational ensemble sampled by the enzyme, which should include productive substrates that are better suited for stabilization of the TS than the average crystal structure. Generating the ensemble from a structure with a bound TS analogue likely helps to enrich such productive

substrates and could partially explain why the KE70 ensemble, which was derived from an unbound structure, led to a lower overall activity improvement. Although the use of an ensemble derived from enzymes in their bound and unbound forms led to activity improvements, one important disadvantage of our approach is that it requires a crystal structure of the original de novo enzyme to generate the ensemble. Since de novo enzymes are typically generated from small, monomeric protein scaffolds whose crystal structures have been determined to high resolution, we do not anticipate that structure determination will create a substantial bottleneck in most cases.

Our results support the idea that to design efficient artificial enzymes, it is essential to consider residual conformational heterogeneity present in the designs and whether it leads to the population of catalytically unproductive conformations. In other words, dynamic aspects of enzyme structure, such as active-site preorganization and enrichment of catalytically competent substrates, must also be considered. This is supported by the fact that the most active designs described here, HG630 and HG649, were ranked lower than less active ones such as HG44 and HG57 based on their predicted ability to stabilize the TS (as reflected by computed energies, Supplementary Table 3). Recently, researchers have proposed that enzyme design should be viewed as a population shift problem, where relative stabilities of conformational substrates are redistributed by the introduction of mutations to stabilize productive substrates.^{15,28} Previous work on the HG series of Kemp eliminases by our team¹⁴ and others¹⁵ demonstrated that directed evolution improves activity through essentially the same mechanism, with higher activity variants having reduced flexibility and greater active-site preorganization, both of which favor the population of catalytically active substrates. The similarity is further highlighted by the fact that our ensemble-based design approach and directed evolution identify activity-enhancing mutations at many of the same positions.

Moving forward, we expect that ensemble-based design will find application in the creation of de novo enzymes for other organic transformations. However, for complex reactions involving multiple steps and transient species, additional developments will be required to make de novo enzyme design robust. For example, improvement of scoring functions used to evaluate sequences is necessary to accurately model forces that stabilize TSs in enzyme active sites, and implementation of multistate design approaches²⁹ for fine-tuning conformational transitions will be required to control progression through the catalytic cycle. We anticipate that ensemble-based design will be extended for achieving the latter objective as it could facilitate identification of sequences that stabilize multiple TSs by using multiple backbone templates from the ensemble. Additionally, we envision using crystallographic ensemble models to further enhance the population of catalytically competent conformations by identifying sequences that can stabilize productive substrates while destabilizing nonproductive ones. The ability to remodel an enzyme conformational landscape³⁰ in this way, using negative design strategies to widen the energy gap between productive and nonproductive conformations, may open the door to the design of more efficient artificial enzymes than previously possible. Beyond the scope of enzyme design, we expect that a similar strategy, which takes advantage of crystallographically derived ensemble models, could find utility in a broad range of

protein design applications. For example, directed evolution following computational design of protein–protein interactions has been shown to enhance affinity by eliminating conformations from the ensemble that are nonproductive for binding.²⁴ Additionally, conformational heterogeneity is detrimental to the functions of computationally designed fluorescent proteins³¹ and ligand-binding proteins.³² Each of these observations suggests a potential application of our proposed approach.

METHODS

Ensemble Generation. Ensembles of backbone templates were generated using the ensemble refinement protocol¹⁸ implemented in the PHENIX macromolecular structure determination software (v1.18.2–3874).³³ In ensemble refinement, local atomic fluctuations are sampled by using MD simulations accelerated and restrained by electron density to produce ensemble models fitted to diffraction data. Briefly, input crystal structures were edited to remove low-occupancy conformers and assign an occupancy of 1.0 to the remaining conformer. Following the addition of riding hydrogens, parallel ensemble refinement simulations were performed using various combinations of the parameters p_{TLS} (0.6, 0.8, 0.9, 1.0), τ_x (0.5, 1.5, 2.0), and $w_{\text{X-ray}}$ (2.5, 5.0, 10.0), where p_{TLS} describes the percentage of atoms included in a translation-libration-screw (TLS) model use to remove the effects of global disorder, τ_x is the simulation time step, and $w_{\text{X-ray}}$ is the coupled temperature bath offset, which controls the extent to which the electron density contributes to the simulation force field such that the simulation runs at a target temperature of 300 K. The ensemble generated from each crystal structure that displayed the lowest R_{free} value was selected for design and analysis (Supplementary Table 1).

Computational Enzyme Design. All calculations were performed with the Triad protein design software³⁴ (Protabit, Pasadena, CA, USA) using a Monte Carlo with simulated annealing search algorithm for rotamer optimization. Individual backbone templates from each structural ensemble were prepared for computational design using the *addH.py* application within Triad, which optimized and renamed hydrogen atoms, assigned protonation state to His residues, flipped His/Asn/Gln side chains if necessary, and rotated hydroxyl, sulfhydryl, methyl, and amino groups in Ser/Thr, Cys, Met, and Lys, respectively.

The Kemp elimination TS was built using parameters described by Privett and co-workers.⁷ For HG3 designs, D127 was used as the catalytic base, and Gln/Asn/Thr/Ser was tested as hydrogen-bond donors at various positions (Supplementary Table 2). For KE70 designs, D16 served as the catalytic base (corresponding to position 17 in the KE70 crystal structure, PDB ID: 3NPV), Q138 as hydrogen-bond donor, and F48 was utilized for introduction of a pi-stacking interaction with the TS (Supplementary Table 9). For both HG3 and KE70 designs, all other positions in the active site were mutated to Gly during theozyme placement to avoid steric clashes with the designed catalytic residues. The 2002 Dunbrack backbone-independent rotamer library³⁵ with expansions of ± 1 standard deviation around χ_1 and χ_2 was used to provide side-chain conformations. A library of TS poses was generated in the active site by targeted ligand placement¹ using the contact geometries listed in Supplementary Table 10. TS pose energies were calculated using a modified version of the Phoenix protein design energy function³⁴ consisting of a Lennard-Jones 12–6 van der Waals term from the Dreiding II force field³⁶ with atomic radii scaled by 0.9, a direction-dependent hydrogen bond term with a well depth of 8.0 kcal mol⁻¹ and an equilibrium donor–acceptor distance of 2.8 Å,³⁷ and an electrostatic energy term modeled using Coulomb's law with a distance-dependent dielectric of 10. During the energy calculation step, TS–side-chain interaction energies were biased to favor interactions that satisfy contact geometries (Supplementary Table 11) by applying an energy benefit of -100 kcal mol⁻¹ as described by Lassila et al.¹ A Triad

patch file for theozyme placement is provided as a Supplementary File.

Next, active-site repacking calculations were performed on the theozyme-containing templates. In these calculations, the TS was translated ± 0.4 Å in each Cartesian coordinate in 0.2 Å increments and rotated 10° about all three axes (origin at TS geometric center) in 5° increments for a total combinatorial rotation/translation search space of 15,625 possible poses. The identities of catalytic residues were fixed and allowed to sample all rotamers of that amino acid type. Residues that were converted to Gly in the theozyme placement step were allowed to sample rotamers of selected amino acids (Supplementary Tables 2 and 9) to form a mostly hydrophobic active site. Side-chain–TS interaction energies were biased to favor contacts satisfying geometries as done during the theozyme placement step (Supplementary Table 11). Rotamer optimization was carried out using the search algorithm, rotamer library, and energy function described above. A Triad patch file for active-site repacking is provided as a Supplementary File.

After active-site repacking, we calculated energy differences between each repacked structure and the corresponding structure in the absence of the TS where all designed residues (including catalytic residues) were converted to Gly. This energy subtraction was done to allow a comparison of energies for sequences across multiple backbone templates. We also measured the angles defining the hydrogen-bond contact between the catalytic base and the TS of the top-scoring sequence obtained from each backbone template. Sequences from the HG3 and KE70 backbone template that gave the lowest energy top-ranked sequence with angles between its catalytic base and the TS within 3 or 3.5% error of the optimal geometries calculated for acetamide dimers²³ (Supplementary Figure 2, Supplementary Table 4), respectively, were selected for library design and cleaning, as described later.

Computational Library Design. Library design was performed with the CLEARSS algorithm³⁸ using the energies obtained after active-site repacking on the single template selected as described earlier. For a specific library size configuration, which is the specific number of amino acids at each position in the protein, the highest probability set of amino acids at each position (based on the sum of their Boltzmann weights) were included in the library. A combinatorial library of approximately 1000 sequences derived from the selected HG3 or KE70 ensemble member was generated. To ensure that the lowest energy rotameric configuration was obtained for each library sequence, we used the *cleanSequences.py* app in Triad to “clean” their structures by optimizing rotamers on the input backbone template using the active-site repacking protocol described above but without modification of the catalytic residue rotameric configuration. To compare energies of “cleaned” sequences, we calculated the energy difference between each optimized structure and the corresponding structure in the absence of the TS where all designed residues (including catalytic residues) were converted to Gly. These energies are reported throughout the figures and text.

Design Filtering. To decrease the number of sequences to test experimentally, “cleaned” structures were filtered by using geometrical criteria. We kept sequences with (i) a TS solvent-accessible surface area lower than 100 or 102 Å² for HG3 and KE70 designs, respectively, and (ii) $\geq 70\%$ of all designed active-site residues predicted to be preorganized, which was determined as those that adopted the same rotamer in the absence and presence of TS. Furthermore, sequences that contained ≥ 5 Met residues or ≥ 2 Cys residues were discarded to reduce conformational heterogeneity of the active site and prevent formation of disulfide bonds, respectively. A final filtering step consisting of short MD simulations was performed for HG3 designs, as described later.

Unconstrained MD Simulation for Filtering of HG3 Designs. All simulations were performed using the Amber 2020 software (<http://ambermd.org/>) with the AMBER19SB force field.³⁹ Long-range electrostatics (> 10 Å) were modeled using the particle mesh Ewald method,⁴⁰ and a time step of 2 fs was used for the production phase. Parameters for the 5-nitrobenzisoxazole substrate were generated using the Antechamber⁴¹ package. “Cleaned” computa-

tional models generated by Triad for the 55 sequences that passed the filtering procedure described earlier were prepared for MD. The TS structure was converted to that of the substrate, hydrogen atoms were added using Reduce,⁴² and each substrate-bound protein molecule was placed in a dodecahedral box with periodic boundary conditions where the distance between the protein surface and the box edges was set to 10 Å. After explicit TIP3P water molecules⁴³ were added, charges on protein atoms were neutralized with Na⁺ and Cl⁻ counterions at a concentration of 0.15 M. The structures were then energy minimized with the steepest descent method to a target maximum force of 1000 kJ mol⁻¹ nm⁻¹. Before equilibration, the system was heated to a target temperature of 300 K for 100 ps. The system was then equilibrated under an NVT ensemble for 100 ps at a temperature of 300 K using a Nose-Hoover thermostat,⁴⁴ while applying position restraints for heavy protein atoms. A second equilibration step under an NPT ensemble was performed for 100 ps with constant pressure and temperature of 1 bar and 300 K, respectively, using the Berendsen barostat.⁴⁵ Following the removal of position restraints, 20 ns production runs under Parrinello–Rahman pressure coupling⁴⁶ were initiated from the final snapshot of the NPT equilibration. After MD, designs were evaluated and ranked according to their catalytic competency, which is the percentage of snapshots in which catalytic contacts between substrate and catalytic side chains were maintained, as calculated using distance and angle metrics listed in *Supplementary Figure 3*.

Protein Expression and Purification. Codon-optimized (*E. coli*) and his-tagged (C-terminus) genes for Kemp eliminases (*Supplementary Tables 12–13*, *Supplementary Figures 6–7*) cloned into the pET-29b(+) vector via *Nde*I and *Xho*I were obtained from Twist Bioscience. Enzymes were expressed in *E. coli* BL21-Gold (DE3) cells (Agilent) using lysogeny broth (LB) supplemented with 100 µg mL⁻¹ kanamycin. Cultures were grown at 37 °C with shaking to an optical density at 600 nm of 0.3–0.7, and protein expression was initiated with 1 mM isopropyl-β-D-1-thiogalactopyranoside. Following incubation at 16 °C for 16 h with shaking (250 rpm), cells were harvested by centrifugation, resuspended in 8 mL of lysis buffer (5 mM imidazole in 100 mM potassium phosphate buffer pH 8.0) supplemented with 1.25 g mL⁻¹ of lyophilized lysozyme and 1 U mL⁻¹ of benzonase nuclease (Merck Millipore), and lysed with an EmulsiFlex-B15 cell disruptor (Avestin). Proteins were purified by immobilized metal affinity chromatography using Ni-NTA agarose (Qiagen) pre-equilibrated with lysis buffer in individual Econo-Pac gravity-flow columns (Bio-Rad). Columns were washed twice, first with 10 mM imidazole in 100 mM potassium phosphate buffer (pH 8.0), and then with the same buffer containing 20 mM imidazole. Bound proteins were eluted with 250 mM imidazole in 100 mM potassium phosphate buffer (pH 8.0) and exchanged into 100 mM sodium phosphate buffer (pH 7.0) supplemented with 100 mM sodium chloride using Econo-Pac 10DG desalting prepak gravity-flow columns (Bio-Rad). Proteins used for crystallization were further purified by gel filtration in 50 mM sodium citrate buffer (pH 5.5) and 150 mM sodium chloride using an ENrich SEC 650 size-exclusion chromatography column (Bio-Rad). Purified samples were concentrated using Amicon Ultracel-3K centrifugal filter units (EMD Millipore) and quantified by measuring the absorbance of the denatured protein in 6 M guanidinium chloride at 280 nm and applying Beer–Lambert's law using calculated extinction coefficients obtained from the ExPAsy ProtParam tool (<https://web.expasy.org/protparam>).

Steady-State Kinetics. All assays were carried out at 27 °C in 100 mM sodium phosphate buffer (pH 7.0) supplemented with 100 mM sodium chloride. Triplicate 200 µL reactions with varying concentrations of freshly prepared 5-nitrobenzisoxazole (Aablocks) dissolved in methanol (10% final concentration, pH of reaction mixture adjusted to 7.0 after addition of methanol-solubilized substrate) were initiated by the addition of 0.02–5.0 or 0.03–16.0 µM for HG or KE70 variants, respectively. Product formation was monitored spectrophotometrically at 380 nm ($\epsilon = 15,800 \text{ M}^{-1} \text{ cm}^{-1}$) in individual 96-well plates (Greiner Bio-One) wells using a Bioteck Synergy H1 multimode plate reader (Agilent). Path lengths for each

well were calculated ratiometrically using the difference in absorbance of 100 mM sodium phosphate buffer (pH 7.0) supplemented with 100 mM sodium chloride and 10% methanol at 900 and 975 nm (27 °C). Linear phases of the kinetic traces were used to measure the initial reaction rates. For cases where saturation was not possible at the maximum substrate concentration tested (2 mM), data were fitted to the linear portion of the Michaelis–Menten model ($v_0 = (k_{\text{cat}}/K_M)[E_0][S]$), and k_{cat}/K_M was deduced from the slope. In all other cases, the data were fitted to the Michaelis–Menten equation to calculate individual k_{cat} and K_M parameters.

Crystallization. Enzyme variants were prepared in 50 mM sodium citrate buffer (pH 5.5) at the concentrations listed in *Supplementary Table 5*. For samples that were cocrystallized with the TS analogue, a 100 mM stock solution of 6-nitrobenzotriazole (6NT, AstaTech) was prepared in dimethyl sulfoxide (DMSO) and diluted 20-fold in the enzyme solutions for a final concentration of 5 mM (5% DMSO). For each enzyme variant, we carried out initial crystallization trials in 15-well hanging-drop format using EasyXtal crystallization plates (Qiagen) and a crystallization screen that was designed to explore the chemical space around the crystallization conditions reported by Broom et al.¹⁴ Crystallization drops were prepared by mixing 1 µL of protein solution with 1 µL of the mother liquor and sealing the drop inside a reservoir containing an additional 500 µL of the mother liquor solution. This procedure was successful for HG185, HG198, and HG630; however, crystallization of HG649 required the identification of a new crystallization condition using sparse matrix screening. We used commercial screening kits (NeXtal) to prepare crystallization drops in 96-well sitting drop plates by mixing 1 µL of the protein solution with 1 µL of the mother liquor and sealing the drop inside a reservoir containing an additional 100 µL of the mother liquor solution. After identifying a suitable mother liquor solution from screening experiments, large crystals suitable for X-ray diffraction experiments were obtained in a 15-well hanging-drop format as described for the other HG variants. The specific growth conditions that yielded the crystals of each HG variant used for X-ray data collection are provided in *Supplementary Table 5*. HG185, HG630, and HG649 crystallized in the absence of the 6NT TS analogue, and the resulting crystals were isomorphous with the HG3 crystal form reported in the PDB (PDB ID: 5RGA and 5RG4). For these variants, crystals with bound 6NT were obtained by soaking the unbound crystals in mother liquor containing 10 mM 6NT for at least 30 min prior to data collection. On the other hand, HG198 could not be crystallized without 6NT present, and the crystals that were obtained belonged to space group *P*1 with three polypeptides in the asymmetric unit. To prepare crystals of HG198 without 6NT bound, we serially soaked 6NT-bound crystals in three drops of crystallization mother liquor without 6NT. Each sequential soaking step was carried out for at least 30 min. After the removal of 6NT by soaking, the *P*1 crystals undergo a transition to space group *P*2₁, with a smaller unit cell and only one molecule per asymmetric unit. Although we could not determine the cause of this unusual change in crystal symmetry upon soaking, we observed that it occurred with a high reproducibility. We measured 10 individual crystals of 6NT-bound HG198, which all belonged to space group *P*1 and were roughly isomorphous. Additionally, we measured four individual crystals of HG198 without 6NT, and we found that all of them demonstrated the transition to monoclinic symmetry.

X-ray Data Collection and Processing. Prior to X-ray data collection, crystals were mounted in polyimide loops and sealed by using a MicroRT tubing kit (MiTeGen). Single-crystal X-ray diffraction data were collected on beamline 8.3.1 at the Advanced Light Source. The beamline was equipped with a Pilatus3 S 6 M detector and was operated at a photon energy of 11,111 eV. Crystals were maintained at 280 K throughout the course of data collection. Each dataset was collected using a total X-ray dose of 50 kGy or less and covered a 180° wedge of reciprocal space. Multiple datasets were collected for each enzyme variant either from different crystals, or if their size permitted, from nonoverlapping volumes of larger crystals, in order to identify optimally diffracting samples. X-ray data were processed with the Xia2 0.5.492 program ([10.1021/jacs.4c00677](https://doi.org/10.1021/jacs.4c00677)).

S0021889809045701),⁴⁷ which performed indexing, integration, scaling, and merging with DIALS.^{48,49} For each dataset, a resolution cutoff was taken where the CC1/2 and $\langle I/\sigma I \rangle$ values for the merged intensities fell to approximately 0.5 and 1.0, respectively. Information regarding data collection and processing is presented in *Supplementary Table 6*. The reduced diffraction data were analyzed with phenix.xtriage to check for crystal pathologies, and no complications were identified.

Structure Determination. We obtained initial phase information for calculation of electron density maps by molecular replacement using the program Phaser,⁵⁰ as implemented in v1.13.2998 of the PHENIX suite.⁵¹ Several different models of HG variants, including crystal structures and design models, were used for molecular replacement. For all datasets except that of HG630 (+) 6NT, we performed iterative steps of manual model rebuilding followed by refinement of atomic positions, atomic displacement parameters, and occupancies using a TLS model, a riding hydrogen model, and automatic weight optimization. For HG630 (+) 6NT, refinement was done as described earlier but without the usage of a TLS model. All model building was performed using Coot 0.8.9.236⁵² and refinement steps were performed with phenix.refine within the PHENIX suite (v1.13–2998).^{51,53} Restraints for 6NT were generated using phenix.elbow,⁵⁴ starting from coordinates available in the Protein Data Bank (PDB ligand ID: 6NT). Further information regarding model building and refinement, as well as PDB accession codes for the final models, is presented in *Supplementary Table 6*.

■ ASSOCIATED CONTENT

Data Availability Statement

Structure coordinates for all HG series Kemp eliminases have been deposited in the RCSB Protein Data Bank with the following accession codes: HG185 (8USK, 8USL), HG198 (8USI, 8USJ), HG630 (8USG, 8USH), HG649 (8USE, 8USF). Source data are provided with this article. Other relevant data are available from the corresponding authors upon reasonable request.

■ Supporting Information

The Supporting Information is available free of charge at <https://pubs.acs.org/doi/10.1021/jacs.4c00677>.

Ensemble refinement results; details for computational design protocols; design filtering metrics; details of crystallographic data collection; sequences of designs; structural analyses of Kemp eliminase variants; structure of 6NT; molecular dynamics filtering; Michaelis–Menten graphs; sequence alignments ([PDF](#))

Triad patch files ([ZIP](#))

■ AUTHOR INFORMATION

Corresponding Authors

Michael C. Thompson — Department of Chemistry and Biochemistry, University of California Merced, Merced, California 95343, United States; Email: mthompson30@ucmerced.edu

Roberto A. Chica — Department of Chemistry and Biomolecular Sciences and Center for Catalysis Research and Innovation, University of Ottawa, Ottawa, Ontario K1N 6N5, Canada; orcid.org/0000-0003-3789-9841; Email: rchica@uottawa.ca

Authors

Rojo V. Rakotoharisoa — Department of Chemistry and Biomolecular Sciences and Center for Catalysis Research and Innovation, University of Ottawa, Ottawa, Ontario K1N 6N5, Canada

Behnoush Seifinoferest — Department of Chemistry and Biochemistry, University of California Merced, Merced, California 95343, United States

Niayesh Zarifi — Department of Chemistry and Biomolecular Sciences and Center for Catalysis Research and Innovation, University of Ottawa, Ottawa, Ontario K1N 6N5, Canada

Jack D.M. Miller — Department of Chemistry and Biomolecular Sciences and Center for Catalysis Research and Innovation, University of Ottawa, Ottawa, Ontario K1N 6N5, Canada

Joshua M. Rodriguez — Department of Chemistry and Biochemistry, University of California Merced, Merced, California 95343, United States

Complete contact information is available at:
<https://pubs.acs.org/10.1021/jacs.4c00677>

Notes

The authors declare no competing financial interest.

Triad patch files are provided with this paper. Requests for the Triad protein design software should be addressed to Protabit (<https://www.protabit.com/>).

■ ACKNOWLEDGMENTS

R.A.C. acknowledges grants from the Natural Sciences and Engineering Research Council of Canada (RGPIN-2021-03484 and RGPAS-2021-00017) and the Canada Foundation for Innovation (26503). R.A.C. and M.C.T. acknowledge a joint grant from the Human Frontier Science Program (RGP0004/2022). This research was enabled in part by support provided by Compute Ontario (www.computeontario.ca) and the Digital Research Alliance of Canada (alliance.can.ca). Beamline 8.3.1 at the Advanced Light Source is operated by the University of California San Francisco with generous support from the National Institutes of Health (R01 GM124149 for technology development and P30 GM124169 for user support), and the Integrated Diffraction Analysis Technologies program of the US Department of Energy Office of Biological and Environmental Research. The Advanced Light Source (Berkeley, CA) is a national user facility operated by Lawrence Berkeley National Laboratory on behalf of the US Department of Energy under contract number DE-AC02-05CH11231, Office of Basic Energy Sciences. The contents of this publication are solely the responsibility of the authors and do not necessarily represent the official views of NIGMS or NIH. The authors wish to thank Natalie K. Goto for critical reading of the manuscript.

■ REFERENCES

- (1) Lassila, J. K.; Privett, H. K.; Allen, B. D.; Mayo, S. L. Combinatorial methods for small-molecule placement in computational enzyme design. *Proc. Natl. Acad. Sci. U. S. A.* **2006**, *103*, 16710–16715.
- (2) Zanghellini, A.; Jiang, L.; Wollacott, A. M.; Cheng, G.; Meiler, J.; Althoff, E. A.; Rothlisberger, D.; Baker, D. New algorithms and an in silico benchmark for computational enzyme design. *Protein Sci.* **2006**, *15*, 2785–2794.
- (3) Rothlisberger, D.; Khersonsky, O.; Wollacott, A. M.; Jiang, L.; DeChancie, J.; Betker, J.; Gallaher, J. L.; Althoff, E. A.; Zanghellini, A.; Dym, O.; Albeck, S.; Houk, K. N.; Tawfik, D. S.; Baker, D. Kemp elimination catalysts by computational enzyme design. *Nature* **2008**, *453*, 190–195.
- (4) Jiang, L.; Althoff, E. A.; Clemente, F. R.; Doyle, L.; Rothlisberger, D.; Zanghellini, A.; Gallaher, J. L.; Betker, J. L.; Tanaka, F.; Barbas, C. F., 3rd; Hilvert, D.; Houk, K. N.; Stoddard, B.

- L.; Baker, D. De novo computational design of retro-aldol enzymes. *Science* **2008**, *319*, 1387–1391.
- (5) Siegel, J. B.; Zanghellini, A.; Lovick, H. M.; Kiss, G.; Lambert, A. R.; St Clair, J. L.; Gallaher, J. L.; Hilvert, D.; Gelb, M. H.; Stoddard, B. L.; Houk, K. N.; Michael, F. E.; Baker, D. Computational design of an enzyme catalyst for a stereoselective bimolecular Diels-Alder reaction. *Science* **2010**, *329*, 309–313.
- (6) Bjelic, S.; Nivón, L. G.; Çelebi-Ölcüm, N.; Kiss, G.; Rosewall, C. F.; Lovick, H. M.; Ingalls, E. L.; Gallaher, J. L.; Seetharaman, J.; Lew, S.; Montelione, G. T.; Hunt, J. F.; Michael, F. E.; Houk, K. N.; Baker, D. Computational design of enone-binding proteins with catalytic activity for the Morita-Baylis-Hillman reaction. *ACS Chem. Biol.* **2013**, *8*, 749–757.
- (7) Privett, H. K.; Kiss, G.; Lee, T. M.; Blomberg, R.; Chica, R. A.; Thomas, L. M.; Hilvert, D.; Houk, K. N.; Mayo, S. L. Iterative approach to computational enzyme design. *Proc. Natl. Acad. Sci. U. S. A.* **2012**, *109*, 3790–3795.
- (8) Blomberg, R.; Kries, H.; Pinkas, D. M.; Mittl, P. R.; Grutter, M. G.; Privett, H. K.; Mayo, S. L.; Hilvert, D. Precision is essential for efficient catalysis in an evolved Kemp eliminase. *Nature* **2013**, *503*, 418–421.
- (9) Yeh, A. H.; Norn, C.; Kipnis, Y.; Tischer, D.; Pellock, S. J.; Evans, D.; Ma, P.; Lee, G. R.; Zhang, J. Z.; Anishchenko, I.; Coventry, B.; Cao, L.; Dauparas, J.; Halabiya, S.; DeWitt, M.; Carter, L.; Houk, K. N.; Baker, D. De novo design of luciferases using deep learning. *Nature* **2023**, *614*, 774–780.
- (10) Khersonsky, O.; Rothlisberger, D.; Wollacott, A. M.; Murphy, P.; Dym, O.; Albeck, S.; Kiss, G.; Houk, K. N.; Baker, D.; Tawfik, D. S. Optimization of the in-silico-designed kemp eliminase KE70 by computational design and directed evolution. *J. Mol. Biol.* **2011**, *407*, 391–412.
- (11) Khersonsky, O.; Kiss, G.; Rothlisberger, D.; Dym, O.; Albeck, S.; Houk, K. N.; Baker, D.; Tawfik, D. S. Bridging the gaps in design methodologies by evolutionary optimization of the stability and proficiency of designed Kemp eliminase KES9. *Proc. Natl. Acad. Sci. U. S. A.* **2012**, *109*, 10358–10363.
- (12) Giger, L.; Caner, S.; Obexer, R.; Kast, P.; Baker, D.; Ban, N.; Hilvert, D. Evolution of a designed retro-aldolase leads to complete active site remodeling. *Nat. Chem. Biol.* **2013**, *9*, 494–498.
- (13) Obexer, R.; Godina, A.; Garrabou, X.; Mittl, P. R.; Baker, D.; Griffiths, A. D.; Hilvert, D. Emergence of a catalytic tetrad during evolution of a highly active artificial aldolase. *Nat. Chem.* **2017**, *9*, 50–56.
- (14) Broom, A.; Rakotoharisoa, R. V.; Thompson, M. C.; Zarifi, N.; Nguyen, E.; Mukhametzhanov, N.; Liu, L.; Fraser, J. S.; Chica, R. A. Ensemble-based enzyme design can recapitulate the effects of laboratory directed evolution in silico. *Nat. Commun.* **2020**, *11*, 4808.
- (15) Otten, R.; Padua, R. A. P.; Bunzel, H. A.; Nguyen, V.; Pitsawong, W.; Patterson, M.; Sui, S.; Perry, S. L.; Cohen, A. E.; Hilvert, D.; Kern, D. How directed evolution reshapes the energy landscape in an enzyme to boost catalysis. *Science* **2020**, *370*, 1442–1446.
- (16) Campbell, E.; Kaltenbach, M.; Correy, G. J.; Carr, P. D.; Porebski, B. T.; Livingstone, E. K.; Afriat-Jurnou, L.; Buckle, A. M.; Weik, M.; Hollfelder, F.; Tokuriki, N.; Jackson, C. J. The role of protein dynamics in the evolution of new enzyme function. *Nat. Chem. Biol.* **2016**, *12*, 944–950.
- (17) Bunzel, H. A.; Anderson, J. L. R.; Hilvert, D.; Arcus, V. L.; van der Kamp, M. W.; Mulholland, A. J. Evolution of dynamical networks enhances catalysis in a designer enzyme. *Nat. Chem.* **2021**, *13*, 1017–1022.
- (18) Burnley, B. T.; Afonine, P. V.; Adams, P. D.; Gros, P. Modelling dynamics in protein crystal structures by ensemble refinement. *Elife* **2012**, *1*, No. e00311.
- (19) Keedy, D. A.; Fraser, J. S.; van den Bedem, H. Exposing Hidden Alternative Backbone Conformations in X-ray Crystallography Using qFit. *PLoS Comput. Biol.* **2015**, *11*, No. e1004507.
- (20) Levin, E. J.; Kondrashov, D. A.; Wesenberg, G. E.; Phillips, G. N., Jr Ensemble Refinement of Protein Crystal Structures: Validation and Application. *Structure* **2007**, *15*, 1040–1052.
- (21) Thompson, M. C. Combining temperature perturbations with X-ray crystallography to study dynamic macromolecules: A thorough discussion of experimental methods. *Methods Enzymol.* **2023**, *688*, 255–305.
- (22) Keedy, D. A.; van den Bedem, H.; Sivak, D. A.; Petsko, G. A.; Ringe, D.; Wilson, M. A.; Fraser, J. S. Crystal cryo cooling distorts conformational heterogeneity in a model Michaelis complex of DHFR. *Structure* **2014**, *22*, 899–910.
- (23) Morozov, A. V.; Kortemme, T.; Tsemekhman, K.; Baker, D. Close agreement between the orientation dependence of hydrogen bonds observed in protein structures and quantum mechanical calculations. *Proc. Natl. Acad. Sci. U. S. A.* **2004**, *101*, 6946–6951.
- (24) Biel, J. T.; Thompson, M. C.; Cunningham, C. N.; Corn, J. E.; Fraser, J. S. Flexibility and Design: Conformational Heterogeneity along the Evolutionary Trajectory of a Redesigned Ubiquitin. *Structure* **2017**, *25*, 739–749.
- (25) Jindal, G.; Warshel, A. Misunderstanding the preorganization concept can lead to confusions about the origin of enzyme catalysis. *Proteins* **2017**, *85*, 2157–2161.
- (26) Maria-Solano, M. A.; Serrano-Hervas, E.; Romero-Rivera, A.; Iglesias-Fernandez, J.; Osuna, S. Role of conformational dynamics in the evolution of novel enzyme function. *Chem. Commun. (Camb)* **2018**, *54*, 6622–6634.
- (27) Yabukarski, F.; Doukov, T.; Pinney, M. M.; Biel, J. T.; Fraser, J. S.; Herschlag, D. Ensemble-function relationships to dissect mechanisms of enzyme catalysis. *Sci. Adv.* **2022**, *8*, No. eabn7738.
- (28) Osuna, S. The challenge of predicting distal active site mutations in computational enzyme design. *WIREs Comput. Mol. Sci.* **2021**, *11*, No. e1502.
- (29) Davey, J. A.; Chica, R. A. Multistate approaches in computational protein design. *Protein Sci.* **2012**, *21*, 1241–1252.
- (30) St-Jacques, A. D.; Rodriguez, J. M.; Eason, M. G.; Foster, S. M.; Khan, S. T.; Damry, A. M.; Goto, N. K.; Thompson, M. C.; Chica, R. A. Computational remodeling of an enzyme conformational landscape for altered substrate selectivity. *Nat. Commun.* **2023**, *14*, 6058.
- (31) Legault, S.; Fraser-Halberg, D. P.; McAnelly, R. L.; Eason, M. G.; Thompson, M. C.; Chica, R. A. Generation of bright monomeric red fluorescent proteins via computational design of enhanced chromophore packing. *Chemical Science* **2022**, *13*, 1408–1418.
- (32) Tinberg, C. E.; Khare, S. D.; Dou, J.; Doyle, L.; Nelson, J. W.; Schena, A.; Jankowski, W.; Kalodimos, C. G.; Johnsson, K.; Stoddard, B. L.; Baker, D. Computational design of ligand-binding proteins with high affinity and selectivity. *Nature* **2013**, *501*, 212–216.
- (33) Liebschner, D.; Afonine, P. V.; Baker, M. L.; Bunkoczi, G.; Chen, V. B.; Croll, T. I.; Hintze, B.; Hung, L.-W.; Jain, S.; McCoy, A. J.; Moriarty, N. W.; Oeffner, R. D.; Poon, B. K.; Prisant, M. G.; Read, R. J.; Richardson, J. S.; Richardson, D. C.; Sammito, M. D.; Sobolev, O. V.; Stockwell, D. H.; Terwilliger, T. C.; Urzhumtsev, A. G.; Videau, L. L.; Williams, C. J.; Adams, P. D. Macromolecular structure determination using X-rays, neutrons and electrons: recent developments in Phenix. *Acta Crystallographica Section D* **2019**, *75*, 861–877.
- (34) Lee, F. S.; Anderson, A. G.; Olafson, B. D. Benchmarking TriadAb using targets from the second antibody modeling assessment. *Protein Eng. Des. Sel.* **2023**, *36*, No. gza013.
- (35) Dunbrack, R. L., Jr. Rotamer libraries in the 21st century. *Curr. Opin Struct Biol.* **2002**, *12*, 431–440.
- (36) Mayo, S. L.; Olafson, B. D.; Goddard, W. A. Dreiding - a Generic Force-Field for Molecular Simulations. *J. Phys. Chem.* **1990**, *94*, 8897–8909.
- (37) Dahiyat, B. I.; Mayo, S. L. Probing the role of packing specificity in protein design. *Proc. Natl. Acad. Sci. U. S. A.* **1997**, *94*, 10172–10177.
- (38) Allen, B. D.; Nisthal, A.; Mayo, S. L. Experimental library screening demonstrates the successful application of computational protein design to large structural ensembles. *Proc. Natl. Acad. Sci. U. S. A.* **2010**, *107*, 19838–19843.

- (39) Lindorff-Larsen, K.; Piana, S.; Palmo, K.; Maragakis, P.; Klepeis, J. L.; Dror, R. O.; Shaw, D. E. Improved side-chain torsion potentials for the Amber ff99SB protein force field. *Proteins* **2010**, *78*, 1950–1958.
- (40) Darden, T.; York, D.; Pedersen, L. Particle mesh Ewald: An N- $\log(N)$ method for Ewald sums in large systems. *J. Chem. Phys.* **1993**, *98*, 10089–10092.
- (41) Wang, J.; Wang, W.; Kollman, P. A.; Case, D. A. Automatic atom type and bond type perception in molecular mechanical calculations. *Journal of Molecular Graphics and Modelling* **2006**, *25*, 247–260.
- (42) Word, J. M.; Lovell, S. C.; Richardson, J. S.; Richardson, D. C. Asparagine and glutamine: using hydrogen atom contacts in the choice of side-chain amide orientation. *J. Mol. Biol.* **1999**, *285*, 1735–1747.
- (43) Jorgensen, W. L.; Chandrasekhar, J.; Madura, J. D.; Impey, R. W.; Klein, M. L. Comparison of simple potential functions for simulating liquid water. *J. Chem. Phys.* **1983**, *79*, 926–935.
- (44) Evans, D. J.; Holian, B. L. The Nose–Hoover thermostat. *J. Chem. Phys.* **1985**, *83*, 4069–4074.
- (45) Berendsen, H. J. C.; Postma, J. P. M.; van Gunsteren, W. F.; DiNola, A.; Haak, J. R. Molecular dynamics with coupling to an external bath. *J. Chem. Phys.* **1984**, *81*, 3684–3690.
- (46) Parrinello, M.; Rahman, A. Polymorphic transitions in single crystals: A new molecular dynamics method. *J. Appl. Phys.* **1981**, *52*, 7182–7190.
- (47) Winter, G.; Lobley, C. M.; Prince, S. M. Decision making in xia2. *Acta Crystallogr. D Biol. Crystallogr.* **2013**, *69*, 1260–1273.
- (48) Winter, G.; Waterman, D. G.; Parkhurst, J. M.; Brewster, A. S.; Gildea, R. J.; Gerstel, M.; Fuentes-Montero, L.; Vollmar, M.; Michels-Clark, T.; Young, I. D.; Sauter, N. K.; Evans, G. DIALS: implementation and evaluation of a new integration package. *Acta Crystallographica Section D* **2018**, *74*, 85–97.
- (49) Evans, P. Scaling and assessment of data quality. *Acta Crystallogr. D Biol. Crystallogr.* **2006**, *62*, 72–82.
- (50) McCoy, A. J.; Grosse-Kunstleve, R. W.; Adams, P. D.; Winn, M. D.; Storoni, L. C.; Read, R. J. Phaser crystallographic software. *J. Appl. Crystallogr.* **2007**, *40*, 658–674.
- (51) Adams, P. D.; Afonine, P. V.; Bunkoczi, G.; Chen, V. B.; Davis, I. W.; Echols, N.; Headd, J. J.; Hung, L. W.; Kapral, G. J.; Grosse-Kunstleve, R. W.; McCoy, A. J.; Moriarty, N. W.; Oeffner, R.; Read, R. J.; Richardson, D. C.; Richardson, J. S.; Terwilliger, T. C.; Zwart, P. H. PHENIX: a comprehensive Python-based system for macromolecular structure solution. *Acta Crystallogr. D Biol. Crystallogr.* **2010**, *66*, 213–221.
- (52) Emsley, P.; Lohkamp, B.; Scott, W. G.; Cowtan, K. Features and development of Coot. *Acta Crystallogr. D Biol. Crystallogr.* **2010**, *66*, 486–501.
- (53) Afonine, P. V.; Grosse-Kunstleve, R. W.; Echols, N.; Headd, J. J.; Moriarty, N. W.; Mustyakimov, M.; Terwilliger, T. C.; Urzhumtsev, A.; Zwart, P. H.; Adams, P. D. Towards automated crystallographic structure refinement with phenix.refine. *Acta Crystallogr. D Biol. Crystallogr.* **2012**, *68*, 352–367.
- (54) Moriarty, N. W.; Grosse-Kunstleve, R. W.; Adams, P. D. electronic Ligand Builder and Optimization Workbench (eLBOW): a tool for ligand coordinate and restraint generation. *Acta Crystallogr. D Biol. Crystallogr.* **2009**, *65*, 1074–1080.